From Structure to Dynamics: Modeling Exciton Dynamics in the Photosynthetic Antenna PS1

B. Brüggemann,[†] K. Sznee,[‡] V. Novoderezhkin,[§] R. van Grondelle,[‡] and V. May*,[†]

Institut für Physik, Humboldt-Universität zu Berlin, Newtonstr. 15, 12489 Berlin, Germany, Division of Physics and Astronomy, Faculty of Sciences and Institute of Molecular Biological Sciences, Vrije Universiteit, De Boelelaan 1081, 1081 HV Amsterdam, The Netherlands, and A. N. Belozersky Institute of Physico-Chemical Biology, Moscow State University, Moscow 119899, Russia

Received: February 18, 2004; In Final Form: June 30, 2004

Frequency domain spectra of the photosystem I (PS1) of *Synechococcus elongatus* are measured in a wide temperature range and explained in an exciton model based on the recently determined X-ray crystal structure. Using the known spatial positions and orientations of the chlorophylls (Chls) the dipole−dipole couplings between the chromophores are calculated. In contrast, the Chl Q_y site energies are determined by a simultaneous fit of low-temperature absorption, linear dichroism, and circular dichroism spectra. The best fit is achieved by an evolutionary algorithm after assigning some chromophores to the red-most states. Furthermore, a microscopically founded homogeneous line width is included and the influence of inhomogeneous broadening is discussed. To confirm the quality of the resulting PS1 model, time-dependent fluorescence spectra are calculated, showing a good agreement with recent experimental results.

I. Introduction

Photosynthesis of plants, green algae, and cyanobacteria is governed by two large pigment−protein complexes, one of them is the photosystem I (PS1). The cyanobacterial PS1 of *Synechococcus elongatus* covers the early events of photosynthesis in one structural unit: the light-induced excitation of chromophore molecules in the antenna and the subsequent transfer of excitation energy to the reaction center part, where charge separation takes place (for an actual overview see ref 1).

Recently, the three-dimensional structure of the PS1 of *S. elongatus* has been published with 2.5-Å resolution[2] (see also Figure 1). For the first time, the spatial orientation and the binding pockets of each chromophore molecule in the core−antenna system could be specified. The PS1 uses 96 chlorophyll (Chl) a molecules and 22 carotenoids as chromophores. Most of the chromophores are arranged in a slightly ringlike structure forming the antenna and surrounding the reaction center. The Chls can be divided into a main part with a Q_y-absorption region around 680 nm (abbreviated as MPChls in the following) and into red Chls absorbing above 700 nm. In the reaction center, six Chls are arranged, including the special pair which is the primary electron donor in the charge-transfer chain (named S1-S2, or P700 according to the main absorption peak). The red Chls have been spectroscopically well characterized.[3] Interestingly, in this region the spectrum of PS1 complexes of different bacteria shows the biggest diversity.[1,4,5] Thus, the assignment of Chls to the red pool is still under discussion.

The availability of the PS1 structure has been complemented by various experiments focusing on the dynamics of excitation energy transfer and relaxation after ultrafast laser pulse excitation. In this connection, transient absorption[6,7] and time-resolved fluorescence[4,8−10] have been measured. These experiments cover a time region extending from intra-MPChl equilibration processes up to excitation trapping in the reaction center.

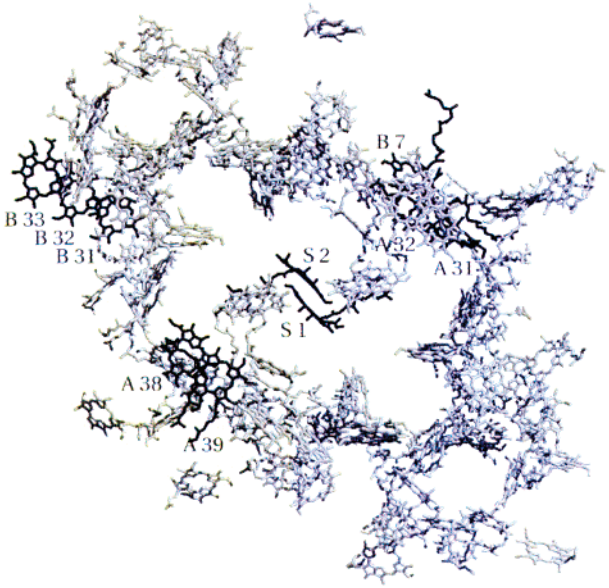

Figure 1. Spatial arrangement of the Chls in the monomeric PS1 complex of *S. elongatus* according to ref 2 (for the labeling of the chromophores see also Table 3 in appendix C).

It is a challenge to relate these spectroscopic data to the structure of the PS1. After publishing the structural data in ref 2, several approaches have been undertaken to find a proper microscopic exciton model for the description of the observed spectroscopic features.[11−14] It is the aim of the present paper to set up a new exciton model for the PSI in the Q_y-absorption region with the specificity of its close relation to our experimental data. In computing the time domain spectra afterward, the quality of the model can be confirmed independently.

[†] Humboldt-Universität zu Berlin.
[‡] Vrije Universiteit.
[§] Moscow State University.

10.1021/jp0401473 CCC: $27.50
Published on Web 08/10/2004

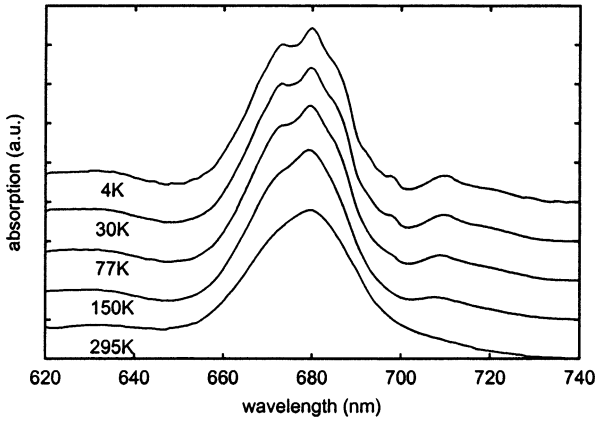

Figure 2. Measured absorption spectrum of the trimeric PS1 complex of *S. elongatus* for temperatures between 4 and 295 K.

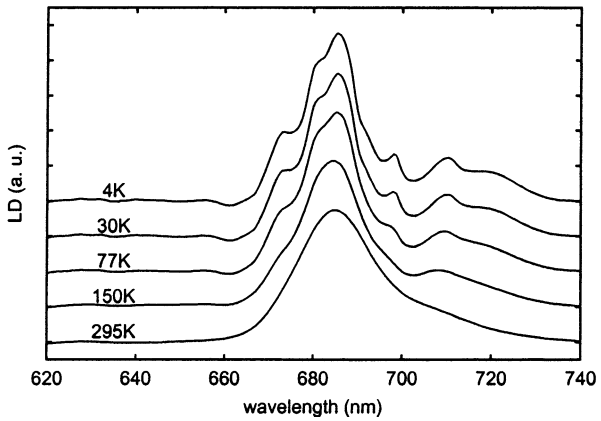

Figure 3. Measured LD of trimeric PS1 complexes of *S. elongatus* for temperatures between 4 and 295 K.

As a starting point for establishing the exciton model, we recorded absorption spectra in a wide temperature range as well as linear dichroism (LD) spectra, which are shortly explained in section II. Combining our data with the circular dichroism (CD) spectra of ref 11 and by using an evolutionary strategy based search for the best fit, we set up our PS1 Q_y-exciton model. This is explained in detail in part A of section IV (the used exciton theory is briefly reviewed in the appendix). Part B of section IV presents the test of the exciton model by calculating the time-dependent fluorescence following photoexcitation with a 100-fs laser pulse. The paper ends with some concluding remarks in section V.

II. Measured Absorption and LD Spectra

Isolated PS I trimeric particles from *S. elongatus* (prepared and stored as described)[4] were embedded in 6.4% (w/v) solution of consumable gelatin. As usual for a low-temperature measurement, the gelatin was diluted with glycerol [final concentration of glycerol was 67% (v/v)] and a buffer containing 20 mM $CaCl_2$, 20 mM $MgCl_2$, 10 mM 2-(*N*-morpholino)ethane sulfonic acid, and 0.05% (w/v) dodecyl-β-D-maltoside at pH 6.5. After relaxation in the dark for about 2 h, the gel has been pressed in two perpendicular directions and expanded freely along the other axis. Measurements were performed in a helium flow Utreks 4.2 K cryostat on samples in acrylic cuvettes with an optical path length of 1 cm. The optical density of the sample at 680 nm was 0.5/cm. The spectra were recorded on a home-built spectrometer, allowing to record absorbance difference (LD) signal simultaneously with the transmission, with 0.5-nm resolution.

The measured linear absorption spectra between 4 and 295 K are given in Figure 2. They agree with spectra of the same complex reported earlier, for example, in ref 11. The LD which has been measured for the first time at low temperatures is shown in Figure 3. It has a remarkably rich structure, with the most striking feature of missing distinct negative peaks in the spectrum. Taking into account the arrangement of the antenna complex in the cellular membrane, one may conclude that the PS1 is optimized to absorb light which is polarized parallel to the membrane plane rather than light which is polarized perpendicular to it.

III. Exciton Model for Time and Frequency Domain Spectra

After the short description of our measurements, let us turn to their interpretation in the framework of an exciton model valid for the Q_y-absorption region. To set up such a model, each Chl has to be characterized by its ground state and by the lowest lying excited Q_y state (see, e.g., ref 15). Because the protein environment differs for different Chls, the Q_y-excitation energies are individually shifted leading to the so-called site energies ϵ_m (the 96 Chls are counted by the site index m, for the concrete labeling see Table 3, cf. also Figure 1).

TABLE 1: Site Energies and Coulombic Interaction Energies for the Chls of the Reaction Center[a]

	S1	S2	S3	S4	S5	S6
S1(P700 A)	−150 (22)	343 (519)	−109	−44	16	7
S2(P700 B)		−150 (29)	−43	−101	6	14
S3(Acc. A)			−115	33	176	−9
S4(Acc. B)				152	−10	216
S5(A_0 A)					−146	2
S6 (A_0 B)						−129

[a] The deviations from the mean Chl energy of 14 841 cm^{-1} (diagonal boxes) and the mutual interaction energies (off-diagonal boxes) are listed (in cm^{-1}). For the special pair (S1, S2), two different sets of site and interaction energies are given (see text).

To compute the related exciton states, it suffices to introduce singly excited states $|m\rangle$ of the PS1. They describe a situation where the mth Chl is in the first excited state but all others are in the ground state. The related PS1 ground state where all chromophores remain unexcited is denoted by $|0\rangle$. The Coulombic interaction among the Chls is mainly of the dipole−dipole type except for the special pair P700 (see Table 1). Here, their compact arrangement requires a certain adjustment of the coupling matrix.

Because the exact positions as well as the orientations of all 96 Chls PS1 are known according to ref 2, all dipole−dipole couplings can be calculated, provided the precise direction of the Q_y-transition dipole moment within the Chls is fixed. In the case of the closely related bacteriochlorophyll molecule, the direction is perpendicular to the x axis of the molecule, which is determined by the direction between the N_A and the N_C atoms of the tetrapyrrole ring. However, for the Chls considered here the angle is smaller than 90°. From LD experiments of isolated Chls, an angle of 70°[16] is determined. A simulation based on different experimental spectra of oriented Chl resulted in an angle of 90°[17] for absorption and 107−109° for emission (adopted to our definition of the x axis). Using time-resolved fluorescence anisotropy and Förster energy transfer simulations, an average angle for absorption and emission of 92−97° has been found in peridinin−Chl a protein.[18] Theoretical calculations favor an angle of 70[19] and 84.1°.[20,21] We will use here an angle of 80°, as will be discussed later. Having specified all the mentioned parameters, the delocalized exciton states

$$|\alpha\rangle = \sum_m C_\alpha(m)|m\rangle \tag{1}$$

and the respective energies $\hbar\Omega_\alpha$ can be calculated. The related expansion coefficients are denoted as $C_\alpha(m)$.

To characterize the coupling to vibrational coordinates of the respective Chl as well as to the protein environment, different types of spectral densities can be introduced (cf., e.g., refs 22 and 23). We will use a description based exclusively on the site-local spectral densities $J_m(\omega)$. They follow from an independent modulation of the Q_y-excitation energy of Chl m[24] and enter the dephasing rates

$$\Gamma_\alpha = \frac{1}{2}\sum_\beta k_{\alpha\beta} + \hat{\Gamma}_\alpha \tag{2}$$

Here, the first term describes energy relaxation with rates $k_{\alpha\beta}$ responsible for transitions from the exciton state $|\alpha\rangle$ to all other states $|\beta\rangle$. The second term accounts for pure dephasing, that is, processes which conserve exciton energy. Although both contributions to Γ_α can be deduced from a microscopic model for the exciton-vibrational coupling,[22,23] the pure dephasing part will be given by a phenomenological expression. According to the experimental findings of ref 26 obtained at low temperatures, we set independent of the actual excitonic state $\hat{\Gamma}_\alpha(T) = \gamma T^{1.3}$, where γ is defined by $\hat{\Gamma}_\alpha(295\ \mathrm{K}) = 275\ \mathrm{cm}^{-1}$. Such a formula defines the main contribution to the broadening of the spectra with rising temperature.

Energy relaxation is governed by the rate constants

$$k_{\alpha\beta} = 2\pi\Omega_{\alpha\beta}{}^2[1 + n(\Omega_{\alpha\beta})]\sum_m |C_\alpha(m)\, C_\beta(m)|^2[J_m(\Omega_{\alpha\beta}) - J_m(\Omega_{\beta\alpha})] \tag{3}$$

with $\Omega_{\alpha\beta} = \Omega_\alpha - \Omega_\beta$ denoting the transition frequencies and $n(\Omega)$ being the Bose distribution. The site-local type of the used spectral densities leads to an overlap expression of the exciton expansion coefficients. To have a concrete expression for $J_m(\omega)$, we follow ref 27 and introduce an overall spectral density $J(\omega)$ which does not depend on the concrete site. If adopted to the PS1, it reads (cf. 1):

$$J_m(\omega) = j_e\sum_{\nu=1}^{5}\eta_\nu \frac{\omega^2}{2\omega_\nu{}^3}\exp(-\omega/\omega_\nu) \tag{4}$$

with $\omega_1 = 10.5\ \mathrm{cm}^{-1}$, $\omega_2 = 25\ \mathrm{cm}^{-1}$, $\omega_3 = 50\ \mathrm{cm}^{-1}$, $\omega_4 = 120\ \mathrm{cm}^{-1}$, and $\omega_5 = 350\ \mathrm{cm}^{-1}$. For all Chls we choose $\eta_\nu = 0.2$ except for those responsible for the red-most state, where we use $\eta_1 = 0.66$, $\eta_2 = 0.66$, $\eta_3 = 2$, $\eta_4 = 10$, and $\eta_5 = 0.8$ to reflect the different experimental findings for the PS1 of *SynechocystisPCC 6803*.[1] The overall coupling factor is set to $j_e = 0.06$ to adjust the dynamics of the whole system (see below). Before commenting briefly on the density matrix theory which includes the energy relaxation and dephasing rates, we list the used formulas for frequency domain spectra.

A. Frequency Domain Spectra. As already stated in the introductory part, different measured spectra have been used to adjust our PS1 excitonic model. First, the linear absorption $A(\omega)$ has been taken. If a regular arrangement of PS1 complexes is assumed, it reads

$$A(\omega) = \frac{4\pi\omega n_{cc}}{\hbar c}\sum_\alpha |\mathbf{d}_\alpha|^2 \frac{\Gamma_\alpha}{(\omega - \Omega_\alpha)^2 + \Gamma_\alpha{}^2} \tag{5}$$

with the volume density n_{cc} of the chromophore complexes and the homogeneous line widths Γ_α according to eq 2. The transition dipole matrix elements into the exciton states $|\alpha\rangle$ read

$$\mathbf{d}_\alpha = \sum_m C_\alpha(m)\mu_m \tag{6}$$

where μ_m denotes the Q_y-transition dipole moment of Chl m with spatial position and orientation according to the PS1 structure. The inhomogeneous broadened absorption follows after a configuration averaging (abbreviated by $\langle ...\rangle_{conf}$ in the following).

The LD which has been measured, too, is the difference in absorption parallel and perpendicular to the axis that is used to orient the molecules. This axis is taken as the z axis perpendicular to the membrane plane, in which the PS1 complexes are integrated. We obtain ($d_{\alpha,x}$, $d_{\alpha,y}$, and $d_{\alpha,z}$ are the Cartesian components of the dipole matrix element)

$$\mathrm{LD}(\omega) = -\frac{4\pi\omega n_{cc}}{\hbar c}\sum_\alpha\left[d_{\alpha,z}{}^2 - \frac{1}{2}(d_{\alpha,x}{}^2 + d_{\alpha,y}{}^2)\right]\frac{\Gamma_\alpha}{(\omega - \Omega_\alpha)^2 + \Gamma_\alpha{}^2} \tag{7}$$

Finally, we quote the expression for the CD

$$\mathrm{CD}(\omega) = -\frac{4\pi\omega n_{cc}}{\hbar c}\sum_\alpha(\mathrm{CD}_\alpha + \mathrm{CD}_\alpha{}^{(chr)})\frac{\Gamma_\alpha}{(\omega - \Omega_\alpha)^2 + \Gamma_\alpha{}^2} \tag{8}$$

with the geometry factor

$$\mathrm{CD}_\alpha = \sum_{mn} C_\alpha(m)\, C_\alpha(n)\mathbf{r}_{m,n}\cdot(\mu_m \times \mu_n) \tag{9}$$

Here, $\mathbf{r}_{m,n}$ connects the centers of the mth and the nth chromophores. For the calculation of the CD spectra, it is important to notice that the Chl molecule exhibits a distinct negative CD spectrum at the Q_y transition.[25] This is taken into account by the additional term $\mathrm{CD}_\alpha{}^{(chr)}$, which is proportional to the negative absorption spectrum of exciton level α ($\mathrm{CD}_\alpha{}^{(chr)} = 0.35|\mathbf{d}_\alpha|^2$). This nonconservative CD spectrum of the PS1 complex in the Q_y region is completed by the conservative part due to the coupling between different Chls.

B. Time-Dependent Fluorescence Spectra. Time and spectrally resolved fluorescence spectra are well suited for an independent test of the used exciton model. To do this, we use the measured data of ref 8. The computations are based on the following formula for the fluorescence spectrum at time t (for details see appendix B and refs 28 and 29):

$$F_\lambda(\omega, t) = -\frac{\omega^3}{8\pi^2\hbar c^3}\left\langle\sum_\alpha \frac{|\mathbf{n}_\lambda\mathbf{d}_\alpha|^2\Gamma_\alpha P_\alpha(t, \mathbf{E})}{(\omega - \Omega_\alpha)^2 - \Gamma_\alpha{}^2}\right\rangle_{conf} \tag{10}$$

The fluorescence spectrum given by this formula is selective with respect to the photon polarization λ (the quantity $\mathbf{n}_\lambda$ is the polarization unit vector). Moreover, F_λ accounts for inhomogeneous broadening via configuration averaging $\langle ...\rangle_{conf}$ with respect to different orientations of the PS1 complexes and with respect to the presence of structural and energetic disorder. Furthermore, the nonequilibrium exciton population $P_\alpha(t, \mathbf{E})$ relaxing to the equilibrium distribution $f(\hbar\Omega_\alpha)$ is included. Its dependence on the exciting field-strength $\mathbf{E}$ indicates the absence of any related perturbational expansion. However, the introduced

formula for F_λ is only valid for those times after optical excitation where all coherences between different exciton states (off-diagonal density matrix elements) died out. And, of course, the upper limit for the use of eq 10 should be a time much smaller than the fluorescence lifetime. In the PS1 the off-diagonal exciton density matrix elements decay substantially faster than the population is redistributed among the diagonal elements if room-temperature conditions are guaranteed (see the succeeding section). Therefore, eq 10 is invalid for the low-temperature region and has to be replaced by the more general expression eq B6 of appendix B.

IV. Computation of Frequency Domain Spectra

To set up the exciton model, a fit of the linear absorption, Figure 2, as well as the LD spectra, Figure 3, and CD spectra (according to ref 3) is done by a certain adjustment of the Chl energies. However, one also has to account for structural and energetic disorder. The presence of disorder has been demonstrated, for example, by hole burning experiments[32] and single molecule spectroscopy[33] and is mainly caused by a certain flexibility of the protein matrix. Consequently, the final aim cannot be the presentation of a single exciton model but rather a whole ensemble of models originated, in the most simple case, by diagonal disorder. Then, the set of *mean* site energies $\{\bar{\epsilon}_m\}$ has to be complemented by related standard deviations $\{\sigma_m\}$. Because it was computationally too expensive to combine the fit of the spectra with a configuration averaging (of some thousand realizations), we choose a different way to account for this important effect. To mimic inhomogeneous line broadening, we introduced an additional state-independent homogeneous broadening $\gamma_0 = 275\ \mathrm{cm}^{-1}$ into the dephasing rate, eq 2. And, the overall coupling factor j_e of the spectral density, eq 4 has been set equal to 0.5. We will call this procedure *disorder-adapted homogeneous broadening*. After an optimal set of site energies has been found, these two additional broadening effects are removed and a configuration averaging is carried out.

A. Spectra Fit by an Evolution Strategy. To adjust the exciton model to the aforementioned spectra, we use the so-called evolution strategy as described in ref 30. In our approach, 20 different realizations of the site energies are generated using an initial set and adding randomly chosen energy deviations. They follow from a normal distribution with a variance of 20 cm^{-1}. Then, the *fitness* of each realization is calculated, and the best five are used to build up the next generation.

As the fitness, we use the mean quadratic deviation of the related experimental spectra from the calculated spectra of absorption, eq 5; LD, eq 7; and CD, eq 8. Additionally, the quadratic deviation of the first derivatives obtained from the measured and calculated spectra is used to reproduce details of the spectra. To determine the fitness, experimental absorption and LD spectra have been taken at 4 K, whereas the CD corresponds to 77 K.

To get the generation following the given one, each site energy is changed with a probability of 20% by a randomly chosen value (from a Gaussian energy distribution of a certain variance), which is called mutation. The mechanism of mutation in the algorithm is complemented by crossover; that is, two of the five distributions are chosen randomly and site by site the energy from either of them is taken by chance. As a third mechanism, double mutation is introduced, where in the same way as described above an amount of energy is added to two neighboring Chls. This procedure accounts for strongly coupled dimers, which may have a similar protein environment and, thus, are similarly shifted in energy. One obtains 10 new realizations from single mutations, 5 from double mutations, and 5 from crossover. On the basis of these new 20 realizations, one may start the procedure again, until a certain optimal value of the fitness parameter is reached (in our case after 500 generations). One may also try to use a larger number of site-energy realizations. However, in the present case this does not lead to improved results but only prolongates the whole procedure. (For the change of the variances of the added random energies we refer to ref 30 for a deeper discussion.) Of course, one cannot expect that the procedure leads to univocal results independent of the initial guess. We will turn back to this question later.

The huge search space as well as the large energy difference between the red Chls and the MPChls does not allow the evolutionary algorithm to achieve a correct assignment of the red Chls. Therefore, an initial condition has been set up with some Chls shifted into the red spectral region. This is, of course, not an unambiguous procedure, and several choices for the energy shift as well as for the set of strongly coupled Chls have been taken. Using only the 4 K absorption and LD spectra, a clear decision remains impossible. However, taking additionally into account the CD spectrum, contributions from the Chls A31-A32-B7, A38-A39, and B37-B38 explain the experimental findings. Following ref 8, the lowest exciton state of the trimer B31-B32-B33 has been adjusted properly to fit the 719-nm absorption (for the identification of the different Chls, see ref 2). For the 710 nm line, we choose the pair A38-A39 and the A31-A32-B7 trimer, which are somewhat lower in energy.

As already discussed in section III, there is a certain ambiguity to chose the position of the Chl Q_y-transition dipole moment within the molecular frame. Using an angle of 70° with respect to the molecular *x* axis, a good fit of LD and absorption spectra could be established as in similar studies on different antennae called CP 29 (cf. ref 31). However, including in the present case the CD data, too, the best fit is obtained with an angle of $80 \pm 5°$.

Figure 4 shows the results of the simultaneous fit of the absorption, LD, and CD spectra (in the low-temperature region). The neglect of vibrational satellites and higher Chl states (e.g., the Q_x state) leads to a slight deviation of the computed spectra from the measured one in the blue region (Figure 4). Using all Chl energies obtained from the fit of the low-temperature spectra (see Table 3 in appendix C), the room-temperature data shown in Figure 4 have been calculated. The absence of the pronounced bleaching of the red states as observed in the experiment can be assigned to a blue shift of the respective red states into the region of MPChl absorption at higher temperatures (ref 4).

Besides the listing of the obtained Chl energies ϵ_m in Table 3, they are also drawn in Figure 5. The values of the various ϵ_m are positioned in Figure 5 relative to the mean PS1 site energy of 14 841 cm^{-1} (the disorder-induced uncertainty amounts $\sigma = 100\ \mathrm{cm}^{-1}$). Moreover, the uncertainty of every Chl energy inherent to the evolutionary algorithm and caused by a different initial guess of the whole set $\{\epsilon_m\}$ (initial-choice uncertainty) has been indicated by error bars. A closer inspection of Figure 5 shows that there are site energies which initial-choice uncertainty is larger than the inhomogeneous broadening (around the Chl A10 and B20, as well as at L02). But one may also find a lot of ϵ_m where inhomogeneous broadening is larger than the initial-choice uncertainty. Hence, there are a number of Chls in the PS1 for which the Q_y-excitation energy can be determined by the described method rather precisely. This underlines that the uncertainty of the whole procedure to find a PS1 exciton model is less arbitrary than one might expect initially.

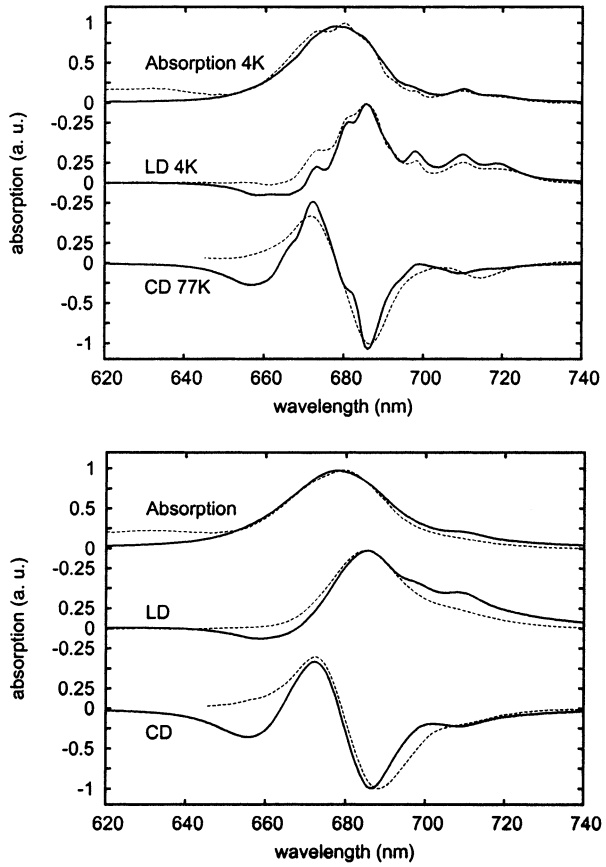

Figure 4. Comparison of the calculated homogeneously broadened absorption, LD, and CD spectra (solid curves) with experimental data (dashed curves). Upper panel, 4 K and the CD spectrum at 77 K; lower panel, 295 K. (The 77 K CD spectrum has been taken from ref 3.)

The reaction center Chls energies (together with their Coulombic interaction energies) are again quoted in Table 2. In the case of the special pair, it is known that the dipole−dipole approximation overestimates the coupling between these Chls. Additionally, the charge transfer state, which is crucial for the biological function of the complex, has an impact.[20,21] To account for these two effects, we decreased the energies of both Chls and their coupling in such a manner that the lowest state of the special pair remains at 698 nm. This choice moves the upper state of the special pair into the main absorption band, and, thus, the energy transfer from the MPChls to the special pair is enhanced.

To compare our results with the previously published ones of refs 11 and 14, we also introduced the respective values into Figure 5. A first view indicates that the data of ref 11 are much closer to ours than those of ref 14. This is not so astonishing because the computations of ref 11 have also been based on measured data. In ref 14, however, quantum chemical calculations have been carried out to get the Q_y-excitation energies of the various Chls, including the coupling to their nearest protein environment. Those energies which belong to the MPChls are in the same range. Highly asymmetric energies in the special pair (710 and 674 nm), however, are favored in ref 14, whereas similar to ref 11 we used for both a value of 681 nm. Another difference is the assignment of the red states. Whereas in ref 14 the lowest state is localized at the special pair, one exciton state lies below the special pair in in ref 11 (located on the dimer A32-B7 at 715 nm) and additionally some weak coupled monomers (B6, B39, L2, P1). The Chls on which the four lowest exciton states are located in our model are given in Table 2.

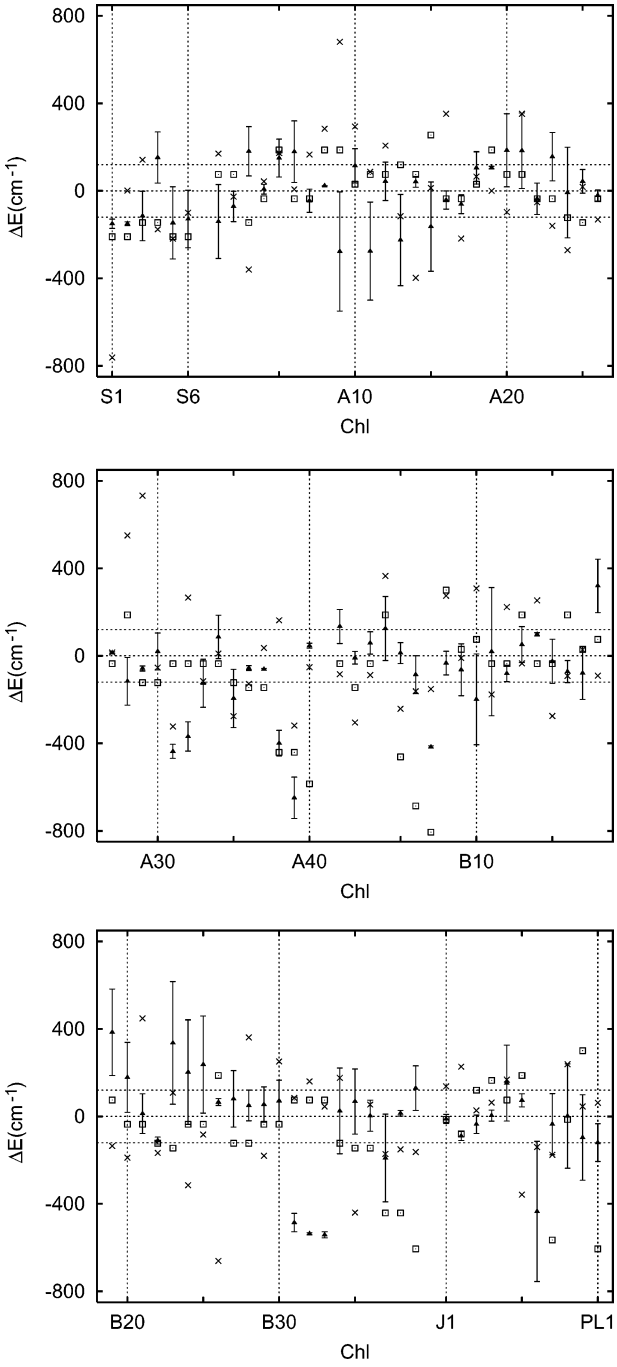

Figure 5. Site energies for the various Chls in the PS1 obtained in the present paper (with error bars) as well as in ref 11 (squares) and ref 14 (crosses). The counting scheme of the Chls follows Table 3. Drawn are the deviations from the mean Chl energy at 14 841 cm^{-1} (the values of ref 14 have been shifted by 880 cm^{-1} to the blue). The horizontal dotted lines indicate the extension of disorder (with σ = 100 cm^{-1}, fwhm = 235 cm^{-1}). The error bars at the values obtained in the present paper give the standard deviation of the site energies obtained from 16 runs of the evolutionary algorithm starting with different initial configurations. The mean standard deviation is $\sigma = 98$ cm^{-1}.

The lowest state of the complex is the lowest lying state of the trimer B31-B32-B33 at 719 nm, followed by the trimer A31-A32-B7 at 710 nm and the dimer A38-A39 at 708 nm. All these states are below the special pair S1-S2 at 698 nm. Whereas the B31-B32-B33 trimer lies at the periphery of the complex, the other low-energy states are located in the vicinity of the reaction center (cf. Figure 1).

TABLE 2: 10 Chls of the PS1 Complex Which Mainly Contribute to the Four Lowest Exciton States α = 1, ..., 4[a]

	α = 1	α = 2	α = 3	α = 4	Δ*E*, cm^{-1}
S1	0	0	0	0.48	−150
S2	0	0	0	0.45	−150
A38	0	0	0.15	0	−399
A39	0	0	0.84	0	−649
A31	0	0.23	0	0	−436
A32	0	0.40	0	0	−369
B7	0	0.33	0	0	−417
B31	0.23	0	0	0	−485
B32	0.49	0	0	0	−536
B33	0.27	0	0	0	−541

[a] Positioned at 719, 710, 708, and 698 nm. Listed are the square of the exciton expansion coefficients $C_\alpha(m)$ as well as the deviation of the site energies from the mean value of 14 841 cm^{-1}.

TABLE 3: Site Energies of the Chls in the PS1 Complex Following from a Simultaneous Fit of Absorption, LD, and CD Spectra[a]

Chl no.	ϵ_n (nm)	ϵ_n (cm^{-1})	Chl no.	ϵ_n (nm)	ϵ_n (cm^{-1})
S1	681	14 691	B3	671	14 899
S2	681	14 691	B4	668	14 965
S3	679	14 726	B5	673	14 853
S4	667	14 993	B6	678	14 755
S5	681	14 694	B7	693	14 424
S6	680	14 712	B8	675	14 808
A1	680	14 701	B9	677	14 777
A2	677	14 770	B10	683	14 642
A3	666	15 021	B11	673	14 860
A4	673	14 848	B12	678	14 760
A5	667	14 991	B13	671	14 892
A6	666	15 019	B14	669	14 939
A7	676	14 795	B15	675	14 815
A8	673	14 864	B16	677	14 769
A9	687	14 564	B17	677	14 762
A10	669	14 955	B18	660	15 160
A11	687	14 565	B19	657	15 225
A12	672	14 884	B20	666	15 019
A13	684	14 616	B21	673	14 853
A14	672	14 882	B22	679	14 730
A15	681	14 677	B23	659	15 176
A16	676	14 799	B24	665	15 043
A17	677	14 779	B25	663	15 077
A18	669	14 946	B26	671	14 906
A19	669	14 947	B27	670	14 921
A20	666	15 026	B28	672	14 891
A21	666	15 024	B29	671	14 895
A22	675	14 804	B30	671	14 911
A23	667	14 996	B31	697	14 355
A24	674	14 833	B32	699	14 304
A25	672	14 884	B33	699	14 300
A26	675	14 820	B34	673	14 865
A27	673	14 855	B35	671	14 909
A28	679	14 724	B36	674	14 843
A29	676	14 783	B37	683	14 651
A30	673	14 861	B38	673	14 855
A31	694	14 404	B39	668	14 969
A32	691	14 472	J01	674	14 829
A33	680	14 715	J02	678	14 751
A34	670	14 927	J03	675	14 805
A35	683	14 646	K01	674	14 844
A36	676	14 785	K02	667	14 993
A37	677	14 779	L01	671	14 914
A38	692	14 442	L02	694	14 406
A39	705	14 192	L03	675	14 805
A40	672	14 886	M01	674	14 842
B1	668	14 975	X01	678	14 744
B2	674	14 832	PL01	679	14 721

[a] Energies are given in nm and cm^{-1}.

B. Dephasing Rates, Stick Spectra, and Delocalization Lengths. The site energies shown in Figure 5 are supplemented by the inverse dephasing rates of every exciton level as drawn in Figure 6. The inverse pure dephasing rate $1/\hat{\Gamma}_\alpha$ as well as the part $1/(\Gamma_\alpha - \hat{\Gamma}_\alpha)$ which is identical with twice the lifetime τ_α caused by energy relaxation processes is shown. According to the used approximation, the former is constant for all exciton levels but decreases strongly with temperature, whereas the latter shows a less pronounced temperature dependence. The variation of $2\tau_\alpha$ over the whole PS1 absorption region is also responsible for the shape of the various computed spectra.

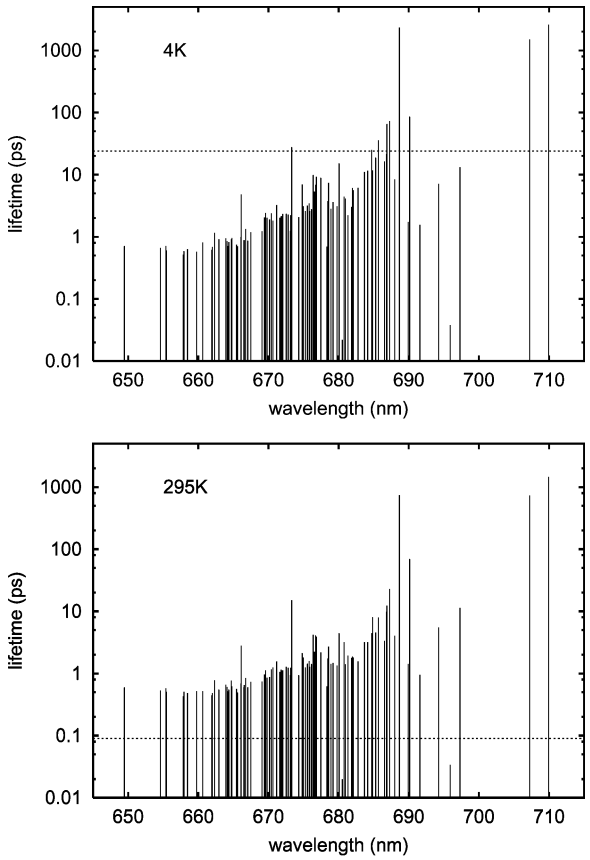

Figure 6. Inverse dephasing rates $2/\sum_\beta k_{\alpha\beta}$ versus wavelength for all PS1 exciton levels. Upper panel, $T = 4$ K; lower panel, $T = 295$ K. The constant inverse pure dephasing rate is given by the dashed line. (Note that the lowest state which is not shown possess an infinitive lifetime because population decay by fluorescence has been neglected.)

The obtained data of the PS1 exciton model are used to draw in the upper part of Figure 7 the stick spectrum of the excitonic dipole moments $|\mathbf{d}_\alpha|$ (divided by the Q_y-transition moment). For comparison, the data are enwraped by the computed 4 K absorption spectrum. The lower part of Figure 7 displays a part of the whole stick spectrum showing the states which are partly localized at the special pair (solid lines with crosses) or at the B31-B32-B33 trimer (dashed lines with stars). For both types, the respective lowest lying localized state has the larger part of the dipole strength. The two higher lying states of the trimer are also localized at the trimer. In contrast, the special pair contributes to a number of higher states, all positioned in the short-wavelength part of the main absorption band.

The spatial delocalization of these states within the PS1 is best demonstrated by the delocalization numbers $N(\alpha) = 1/\sum_m |C_\alpha(m)|^4$.[34] They are drawn versus $\hbar\Omega_\alpha$ in Figure 8. The mean value of this number amounts 4.99, with deviations to higher numbers in the main part of the absorption band and deviations to lower numbers at the red and blue edges of the spectrum. It is important to discuss here the $N(\alpha)$ for a single PS1 and not the configuration averaged delocalization numbers. Only the first carries information on the spatial extension of

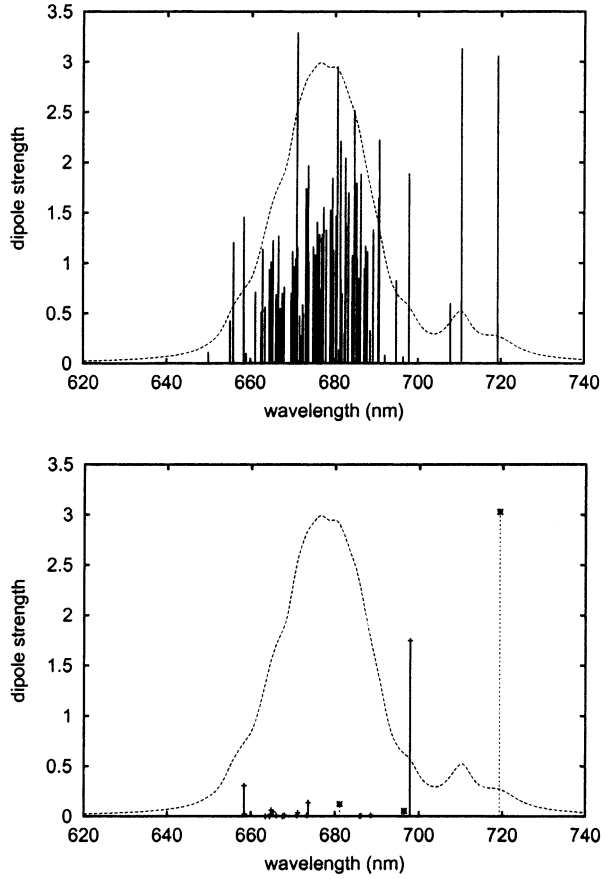

Figure 7. Stick spectrum of the PS1 Q_y absorption. The upper part shows the complete spectrum. The lower part displays the contribution of the special pair S1-S2 (solid lines with crosses) and the trimer B31-B32-B33 (dashed lines with stars). The calculated absorption spectrum at 4 K is shown by the dashed line in both figures.

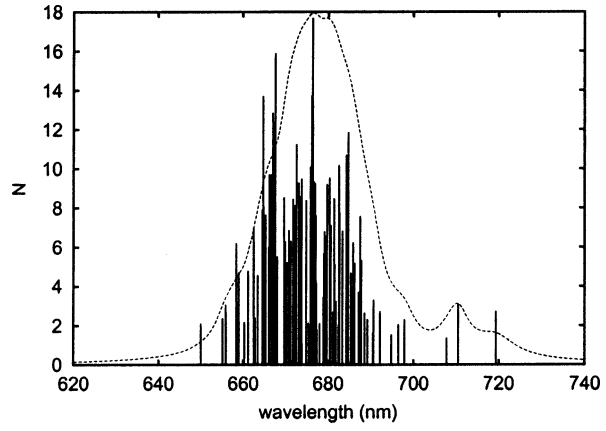

Figure 8. Delocalization length $N(\alpha)$ of all exciton states versus wavelength (average delocalization length amounts 4.99, calculated 4 K absorption spectrum is shown as a dashed line).

exciton states in a particular PS1 complex of the whole ensemble [$\langle N(\alpha)\rangle_{\mathrm{conf}}$ would hide this].

C. Direct Account of Disorder. Let us turn to a direct consideration of disorder effects on the computed frequency domain spectra. As already explained, this was not possible when fitting the spectra in the framework of the evolutionary algorithm. Instead, we introduced a model with disorder-adapted homogeneous broadening. In the following, on the basis of the site energies obtained in this way, we will remove the artificial part of the homogeneous broadening and carry out a configurational averaging. This approach should mainly be understood as a consistency check. If the newly computed spectra do not deviate too much from the already calculated ones, the use of adapted homogeneous broadening may be justified. The check has been carried out in concentrating on disorder with respect to the site energies by providing a Gaussian distribution of them with a variance σ of 100 cm^{-1}. It results in a full width at half-maximum (fwhm) of the disorder of 235 cm^{-1}, which is an upper limit of the disorder in this complex. For the trimer B31-B32-B33, which we assigned to the red-most lying absorption band, we used a different spectral density as discussed above, and we somewhat increased the effect of the disorder by setting $\sigma = 150$ cm^{-1}. Moreover, the increased homogeneous broadening used in the fitting procedure is removed and we set $\gamma_0 = 0$ and $j_e = 0.06$.

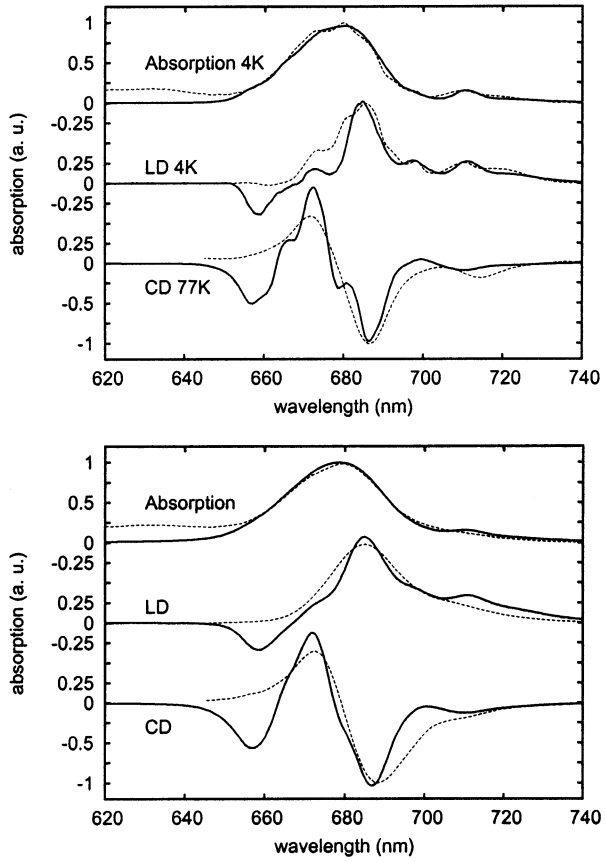

Figure 9. Comparison of calculated spectra (solid curves) including inhomogeneous broadening with experimental data (dashed curves). Upper panel, $T = 4$, 77 K; lower panel, $T = 295$ K. (Gaussian distributed diagonal disorder of 100 cm^{-1} has been used and an averaging over 10^5 realizations was carried out.)

The spectra shown in Figure 9 have been obtained by averaging over up to 10^5 disorder realizations of the whole PS1 (the room temperature spectra follow from the same disorder distribution as the low-temperature data). When comparing the calculated spectra of Figure 9 with those of Figure 4, it becomes obvious that there are no dramatic deviations between them (the coincidence of the computed spectra with the measured ones in Figure 4 is a little bit better than in Figure 9 because the former directly follow from the fitting procedure). We consider this good agreement between spectra with adopted homogeneous broadening and disorder averaged spectra as a justification of the used approach. Needless to say, a fitting procedure including disorder averaging would be more satisfactory, but at the moment it is numerically too expensive.

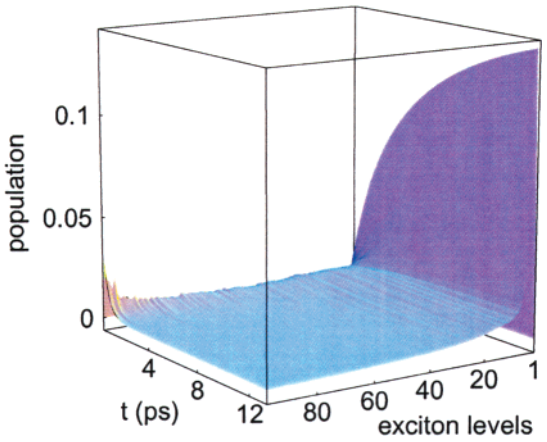

Figure 10. Disorder and orientational averaged exciton populations $\langle P_\alpha(t)\rangle_{conf}$ after a 100-fs pulse excitation at a 650-nm wavelength versus time and for all 96 exciton levels (T = 295 K, averaging over 100 different spatial orientations and realizations of diagonal disorder; note the quasi-continuous representation of the population versus α).

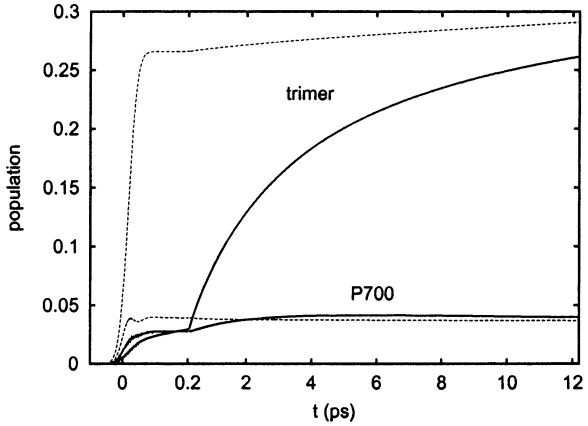

Figure 11. Redistribution of normalized Q_y-state populations at the special pair P700 and the red-lying trimer B31-B32-B33 after an excitation with an 100-fs pulse. Solid curves, excitation at a 650-nm wavelength (T = 295 K); dashed curves, excitation at a 710-nm wavelength (T = 295 K). An averaging over 100 different spatial orientations and realizations of diagonal disorder has been carried out. (Note the use of two different time scales. The profile of the exciting pulse is shown by the light dashed curve.)

V. Computation of Time-Dependent Fluorescence Spectra

Different ultrafast spectroscopic experiments have been reported for the PS1, among them pump−probe experiments[6,7,35] and the detection of time-resolved fluorescence.[8−10,35,36] To calculate the transient absorption of a pump−probe experiment, the two-exciton states, which give rise to excited-state absorption, have to be considered. This has been done for smaller complexes, for example, the antenna systems LH1,[37] LH2,[24,38,39] and LHCII,[40] but it is computationally expensive for the PS1 complex (in the easiest description it requires $96 \times 95/2 = 4656$ states).

Therefore, we restrict our calculations to time and spectrally resolved fluorescence, which only requires studying the (single-) exciton dynamics after laser pulse excitation. (As an additional restriction, our simulation neglects excitation energy trapping in the reaction center.) Albeit, 96 exciton levels have to be included in the simulation, and it was possible to account for static disorder (as discussed in the foregoing section) as well as random spatial orientation. But this was not possible by a direct averaging of the respective spectrum to be calculated. Because the field strength of the exciting laser pulse enters the density matrix equations (A1), we have to solve them repeatedly with randomly rotated PS1 and randomly chosen deviations of the site energies from their respective mean values. This need to propagate the full density matrix for every disorder configuration over the whole time region of interest restricts the number of considered configurations. Although 100 different configurations could only be included, we believe that an estimate of disorder effects that is not too rough has been achieved.

Figure 10 displays the disorder and orientational averaged exciton populations $\langle P_\alpha(t)\rangle_{conf}$ versus time for all 96 exciton states of the PS1. The results have been obtained after excitation with a linearly polarized 100-fs (fwhm) pulse with a wavelength of 650 nm. The pulse excites a certain range of exciton states at the high-energy part of the spectrum. The whole population relaxes down to the lowest-lying 30 levels with the majority of the population in the first exciton level $\hbar\Omega_1$ (the population $\langle P_1\rangle_{conf}$ becomes visible by the gray background in Figure 10). After about 20 ps, the whole exciton system has been equilibrated.

In Figure 11, the site-population $\langle P_m(t)\rangle_{conf}$ of two groups of Chls, the special pair P700, and the trimer B31-B32-B33, which gives rise to the red-most state, are drawn for pump pulses with 650 and 710 nm wavelengths. The populations are normalized by the total exciton-state population $\sum_\alpha\langle P_\alpha\rangle_{conf}$ achieved by the laser pulse action. The pulse at 710 nm directly excites the special pair and the trimer. In contrast to this, the main absorption of the 650-nm pulse is in the MPChl region, and the trimer and the special pair are mostly populated by transfer of the excitation energy.

A. Decay Associated Spectra (DAS). In a next step, we calculate the fluorescence of the PS1 complex as measured in ref 8 for these two excitation wavelengths and at room temperatures. The latter instance justifies the use of eq 10 for the fluorescence spectrum because in this temperature region the pure dephasing rate is about 1 order of magnitude larger than dephasing caused by energy relaxation (cf. Figure 6 and appendix B). As in similar experiments, the fluorescence is detected at a polarization turned 90° with respect to the pump pulse polarization. To come into close contact to the experiments of ref 8, we treat the calculated time and spectrally resolved fluorescence data in the same way by constructing so-called DAS. Therefore, the fluorescence spectrum $F(\omega, t)$ is fitted by multiexponential functions $F_\lambda(\omega_k, t) = \sum_l F_l(\omega_k)\exp(-t/\tau_l)$ at a number of chosen frequencies ω_k. The $F_l(\omega_k)$ drawn versus the discrete frequencies ω_k represent the DAS for the given set of time constants τ_l. The fitting procedure is carried out by using the nonlinear multidimensional least-squares fitting Levenberg−Marquardt algorithm.[41]

Figure 12 displays the DAS $F_k(\omega_l)$ for the excitation wavelength of 650 nm with an initial time fixed just at the end of the pump pulses (of 100-fs duration). The 20 different frequencies ω_k follow from an equidistant distribution of 20 wavelengths between 650 and 750 nm. For the excitation with a 650-nm pulse, five time constants τ_l are sufficient to achieve a good fit of the calculated fluorescence spectra.[42] The interpretation is straightforward. The fast components of 0.4 and 1.0 ps describe the equilibration within the MPChls. The 1.0-ps component already shows some energy transfer to the red states, mostly by local energy relaxation from the directly excited higher states to the lower exciton states of the red Chls. The 3.4-ps component characterizes the equilibration of the MPChls with the red Chls at 710 nm, whereas the 10 ps component shows the equilibration of the MPChls with the red Chls at 719 nm. Slower processes could not be found in our simulations,

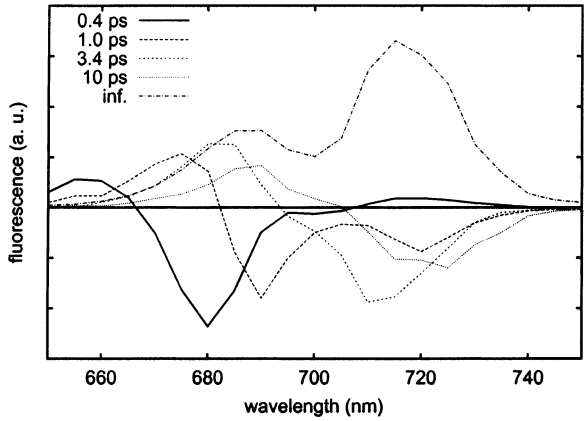

Figure 12. DAS of the fluorescence after a 100-fs excitation at 650 nm at (T = 295 K, averaging over 100 different spatial orientations and realizations of diagonal disorder).

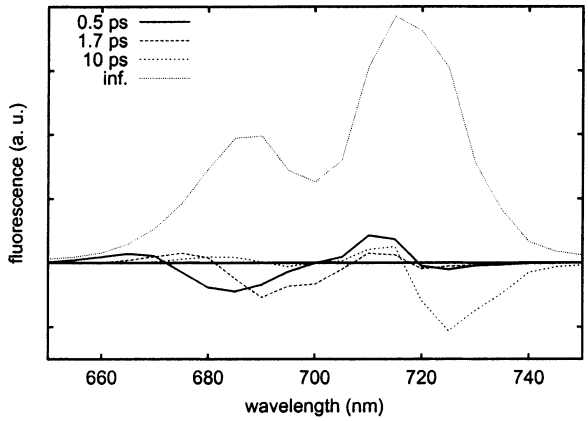

Figure 14. DAS of the fluorescence after a 100-fs excitation excitation at 710 nm (T = 295 K, averaging over 100 different spatial orientations and realizations of diagonal disorder).

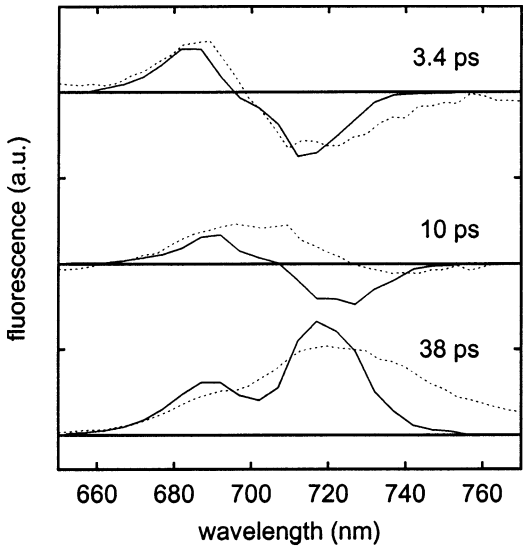

Figure 13. Comparison between experimental (dotted) and simulated (solid) DAS of the fluorescence after a 100-fs excitation at 650 nm (T = 295 K). The experimental DAS at 38 ps is compared with the computed one at infinite time. (All simulated spectra have been shifted to the red by 2 nm.)

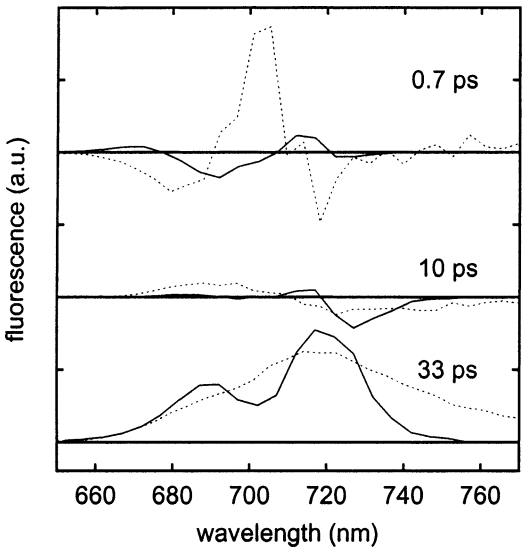

Figure 15. Comparison between experimental (dotted) and simulated (solid) DAS of the fluorescence after a 100-fs excitation at 710 nm (T = 295 K). For the fastest experimental time, the sum of the calculated DAS with the time constants 0.5 and 1.7 ps has been used. The experimental DAS at 33 ps is compared with the computed one at infinite time. (All calculated spectra have been shifted to the red by 2 nm.)

because trapping processes were not included. The totally equilibrated fluorescence is given by the last component with an infinitive lifetime.

A comparison of the calculated DAS of Figure 12 with the experimental ones from ref 8 is shown in Figure 13. Drawn are the 3.4-ps and the 10-ps components as well as the totally equilibrated fluorescence component which has been identified with the 38-ps component of ref 8. Note that the calculated spectra have been shifted to the red by 2 nm to account for fast intramolecular relaxation. The fastest experimental component is that at 3.4 ps, which perfectly agrees with our simulation (upper panel of Figure 13). Because we did not include vibrational sidebands of the Chls, the calculated spectra do not extend into the red as much as the experimental ones do. The experimental 10-ps component consists of a transfer and a trapping part, and if the trapping part is subtracted (not shown), it agrees rather well with the computed DAS. The agreement with the slowest measured component of 38 ps (trapping component) is reasonable, although the experimental DAS extends more to the red for reasons discussed above.

Finally, we compare computed DAS with spectra measured for an excitation wavelength at 710 nm in the region of the red Chls. The population dynamics (not shown) gives a sharp rise in that region, and does not change much afterward. Figure 14 shows the calculated DAS using four time constants τ_l. The fastest component with a time constant of 0.5 ps is originated by thermally excited transfer from the 710-nm Chl states to the main absorption band. The 1.7-ps component consists of a transfer from the 710-nm states to the red part of the MPChl states and an equilibration between the MPChl states. This is followed by a slower equilibration from the 710-nm states to the 719-nm state with 10 ps. The comparison with the experimental DAS given in Figure 15 shows that at 0.7 ps a fast process has been observed in the experiment which is not included in the simulations. Internal vibrational relaxation within the Chls might be an explanation. Besides this, the agreement is of the same quality as that of Figure 15. For the 10-ps component, the match of the measured data could be improved by using an averaging over a larger number of complexes.

Similar calculations as mentioned here have been also carried out in ref 13, partially based on a Förster transfer description of exciton dynamics but without any direct comparison with experimental data. Although the main results agree with ours, we consider our data as more reliable, in particular on a

subpicosecond time scale. Here, the finite 100-fs laser pulse excitation and the sophisticated density matrix propagation accounting for delocalized states and excitonic coherences have a considerable influence on the dynamics.

VI. Conclusions

The structural data for the PS1 complex of *S. elongatus* distributed by ref 2 enables one to construct an exciton model for the Q_y-absorption region and to explain respective frequency and time domain spectra. In particular, this helps to identify the energy transfer pathways used to transport excitation energy after photoabsorption to the reaction center in this large core antenna complex.

So far different approaches have been undertaken to get such a proper exciton model.[11,12,14] All have in common using the structural data to fix individual transition dipole moments and inter-Chl Coulombic couplings. The differences, however, lie in the way the site energies of the single Chls are determined, either by semiempirical quantum chemical calculations[14] or by fitting linear spectra.[11] We followed the latter approach but included low-temperature data where the earlier treatment of ref 11 fails. Moreover, the accuracy of our data should be higher because we first recorded absorption and LD spectra over a broad temperature range and second fitted the 4 K spectra (also including the 77 K CD spectrum taken from ref 11) with the aid of an evolutionary strategy.[30] The uncertainty of this approach could be qualified by demonstrating that there are a number of Chls for which the Q_y-excitation energy can be determined rather precisely. But there are also Chls characterized by a large uncertainty with respect to their excitation energy. We underlined the fact that there does not exist a unique exciton model because structural and energetic disorder are present. Although it was not possible to include configuration averaging within the fit procedure, we demonstrated by the inclusion of disorder after fixing the Chl energies that our *disorder-adapted homogeneous broadening* is rather consistent.

In a next step, the quality of our PS1 exciton model was checked independently by the computation of time-domain spectra. For this reason, we took the time-dependent fluorescence spectra measured in ref 8 after photoexcitation. The experimental data could be well-reproduced. However, we do not consider this as a complete confirmation of our exciton model but as a hint to have a reasonable data set for further computations. Such calculations will be done in ref 43 where we discuss the possibility to use a tailored laser pulse to localize excitation energy in a particular Chl of the PS1 at a certain time (see also our recent results on the FMO complex in ref 44).

Acknowledgment. We thank B. Gobets for useful discussions and the experimental fluorescence data and E. Schlodder for the CD spectra. The cooperation of the group of V. May and the group of R. van Grondelle has been supported by the ESF ULTRA program. Financial support by the Deutsche Forschungsgemeinschaft, Sonderforschungsbereich 450 (B.B.) is gratefully acknowledged.

Appendix A: Exciton Density Matrix

Density matrix theory appropriate for the description of excitation energy dynamics in pigment protein complexes has been described at different places.[22−24] For the present purposes, we may neglect two-exciton contributions and can concentrate on the (reduced) single-exciton density matrix $\rho_{\alpha\beta}(t) = \langle\alpha|\hat{\rho}(t)|\beta\rangle$, with $\hat{\rho}$ denoting the (reduced) exciton density operator. Quantities being off-diagonal with respect to the exciton states $|\alpha\rangle$, eq 1, and the ground-state $|0\rangle$ (so-called coherences) are given by $B_\alpha(t) = \langle\alpha|\hat{\rho}(t)|0\rangle \equiv \langle 0|\hat{\rho}(t)|\alpha\rangle^*$. Finally, the ground-state density matrix (population) reads $P_g(t) = \langle 0|\hat{\rho}(t)|0\rangle$. If necessary, $P_g(t)$ can be replaced by $1 - \sum_\alpha \rho_{\alpha\alpha}$.

We assume a weak coupling to the vibrational degrees of freedom and use the following equations of motion (see, e.g., refs 22 and 23):

$$\frac{\partial}{\partial t}\rho_{\alpha\beta} = -i\Omega_{\alpha\beta}\rho_{\alpha\beta} + \delta_{\alpha\beta}\sum_\gamma(-k_{\alpha\gamma}\rho_{\alpha\alpha} + k_{\gamma\alpha}\rho_{\gamma\gamma}) - (1-\delta_{\alpha\beta})(\Gamma_\alpha + \Gamma_\beta)\rho_{\alpha\beta} + \frac{i}{\hbar}\mathbf{E}(t)(\mathbf{d}_\alpha B_\beta^* - \mathbf{d}_\beta^* B_\alpha) \quad \text{(A1)}$$

and

$$\frac{\partial}{\partial t}B_\alpha = -i(\Omega_\alpha - i\Gamma_\alpha)B_\alpha + \frac{i}{\hbar}\mathbf{E}(t)(\mathbf{d}_\alpha P_g - \sum_\beta \mathbf{d}_\beta \rho_{\alpha\beta}) \quad \text{(A2)}$$

These exciton density matrix equations account for dephasing and energy relaxation as introduced in eqs 2 and 3, respectively, and include the coupling to the radiation field.

Appendix B: Time and Frequency Resolved Fluorescence

In the following, we give a brief explanation of the formula used in section IIIB to compute the luminescence at time t and per frequency and solid angle interval. The standard description is based on an expansion with respect to the pump field as well as the quantized field of the emitted photons.[28] Here, we only take an expansion with respect to the latter type of field but calculate the complete pump-field driven dynamics of the system.

The coupling of excitons to the quantized radiation field are taken as

$$H_{x-\mathrm{rad}} = -i\hbar\sum_{\lambda,\mathbf{k}}\hat{h}_{\lambda\mathbf{k}}(\alpha_{\lambda\mathbf{k}} + \alpha_{\lambda-\mathbf{k}}^+) \quad \text{(B1)}$$

where $a_{\lambda\mathbf{k}}$ and $\alpha_{\lambda-\mathbf{k}}^+$ denote the annihilation and creation operator, respectively, of a photon with polarization λ and wavevector $\mathbf{k}$. The quantities

$$\hat{h}_{\lambda\mathbf{k}} = \sum_\alpha g_{\lambda\mathbf{k}}(\alpha)|\alpha\rangle\langle 0| + \mathrm{hc} \quad \text{(B2)}$$

include the transition operators $|\alpha\rangle\langle 0|$ into the single exciton manifold and the coupling constant (used in the dipole approximation)

$$g_{\lambda\mathbf{k}}(\alpha) = \sqrt{\frac{\pi}{2V\hbar\omega_\mathbf{k}}}\Omega_\alpha\,\mathbf{n}_{\lambda\mathbf{k}}\mathbf{d}_\alpha \quad \text{(B3)}$$

The single PS1 emission rate given per frequency and solid angle interval as well as at polarization λ is obtained from the quantity $R_{\lambda\mathbf{k}} \equiv R_\lambda(\omega)$ according to (V is the normalization volume for the quantized radiation field)

$$F_\lambda(\omega) = \frac{V\omega^2}{(2\pi c)^3}R_\lambda(\omega) \quad \text{(B4)}$$

The rate $R_{\lambda\mathbf{k}}$ follows as the number of photons emitted per time into the state with polarization λ and wavevector $\mathbf{k}$. Because emission appears into the photon vacuum, we may set $R_{\lambda\mathbf{k}} =$

$\partial N_{\lambda\mathbf{k}}/\partial t$, where $N_{\lambda\mathbf{k}} = \mathrm{tr}\{\hat{W}(t)a^{+}_{\lambda\mathbf{k}}a_{\lambda\mathbf{k}}\}$ is the expectation value of the photon number at time t. The trace covers the state space of the radiation field and of the excitons. Consequently, the statistical operator $\hat{W}(t)$ has already been reduced to this subspace via removing all vibrational degrees of freedom. The initial value of $\hat{W}$ is given by $|0\rangle\langle 0| \times |\mathrm{vac}\rangle\langle\mathrm{vac}|$, with the first part projecting on the PS1 ground state and the second one on the radiation field vacuum.

Then, a second-order calculation of the rate with respect to the exciton−photon coupling yields

$$R_{\lambda\mathbf{k}} = -2\,\mathrm{Re}\int_{t_0}^{t} \mathrm{d}\bar{t}\; \mathrm{e}^{-i\omega_{\mathbf{k}}(t-\bar{t})} \times \mathrm{tr}_x\{\hat{h}_{\lambda\mathbf{k}}\mathscr{U}_0(t-\bar{t})\hat{h}_{\lambda-\mathbf{k}}\hat{\rho}(\bar{t};\mathbf{E})\} \quad \text{(B5)}$$

In this formula, the density operator $\hat{\rho}$ has to be propagated according to the eqs A1 and A2, including the exciting external field $\mathbf{E}$. A density operator propagation from $\bar{t}$ to t in the absence of $\mathbf{E}$ is described by the time-evolution superoperator $\mathscr{U}_0(t-\bar{t})$. This all yields (note $\tau = t - \bar{t}$)

$$R_{\lambda\mathbf{k}} = -2\,\mathrm{Re}\sum_{\alpha,\beta} g_{\lambda-\mathbf{k}}{}^{*}(\alpha)\, g_{\lambda\mathbf{k}}(\beta) \times \int_0^{t-t_0} \mathrm{d}\tau\; \mathrm{e}^{-i(\omega_{\mathbf{k}}-\Omega_\beta-i\Gamma_\beta)\tau}\rho_{\alpha\beta}(t-\tau) \quad \text{(B6)}$$

If inserted into eq B4, the emission spectrum measured under ideal time and frequency resolution is obtained (cf., e.g., ref 29).

The formula for $R_{\lambda\mathbf{k}}$, eq B6, displays a memory effect with respect to the exciton dynamics (during and after photoexcitation) with a duration determined by the inverse dephasing rates Γ_β, eq 2. For the system under consideration and at room-temperature conditions, the pure dephasing rate $\hat{\Gamma}_\alpha$ dominates the total rate Γ_α, eq 2 (cf. also Figure 6). This results in a faster decay of the off-diagonal density matrix elements $\rho_{\alpha\beta}$ compared to the arrival of the diagonal matrix elements $P_\alpha = \rho_{\alpha\alpha}$ at an equilibrium distribution $f(\hbar\Omega_\alpha)$ across the exciton levels.

Therefore, when considering a time region t, where the exciting pulse is already over for a time interval compared or larger to the largest $1/\hat{\Gamma}_\beta$, we can assume that the off-diagonal elements of the exciton density matrix died out; that is, we may set $\rho_{\alpha\beta}(t-\tau) \approx \delta_{\alpha\beta}P_\alpha(t)$. The neglect of τ in P_α is justified by the slow population redistribution compared to $1/\hat{\Gamma}_\beta$. Using the same argument, we may extend the τ integral up to $t - t_0 \rightarrow \infty$, which finally gives eq 10.

References and Notes

(1) Gobets, B.; van Grondelle, R. *Biochim. Biophys. Acta* **2001**, *80*, 1507.

(2) Jordan, P.; Fromme, P.; Witt, H. T.; Klukas, O.; Saenger, W.; Krauβ, N. *Nature* **2001**, *411*, 909.

(3) Pålsson, L.-O.; Dekker, J. P.; Schlodder, E.; Monshouwer, R.; van Grondelle, R. *Photosynth. Res.* **1996**, *48*, 239.

(4) Gobets, B.; van Stokkum, I. H. M.; Rögner, M.; Kruip, J.; Schlodder, E.; Karapetyan, N. V.; Dekker, J. P.; van Grondelle, R. *Biophys. J.* **2001**, *81*, 407.

(5) Gobets, B.; van Amerongen, H.; Monshouwer, R.; Kruip, J.; Rögner, M.; van Grondelle, R.; Dekker, J. P. *Biochim. Biophys. Acta* **1994**, *75*, 1188.

(6) Melkozernov, A. N.; Lin, S.; Blankenship, R. E. *Biochemistry* **2000**, *39*, 1489.

(7) Melkozernov, A. N.; Lin, S.; Blankenship, R. E. *J. Phys. Chem. B* **2000**, *104*, 1651.

(8) Gobets, B.; van Stokkum, I. H. M.; van Mourik, F.; Rögner, M.; Kruip, J.; Schlodder, E.; Dekker: J. P.; van Grondelle, R. *Biophys. J.* **2003**, *85*, 3883.

(9) Pålsson, L.-O.; Tjus, S. E.; Andersson, B.; Gillbro, T. *Chem. Phys.* **1995**, *194*, 291.

(10) Kennis, J. T. M.; Gobets, B.; van Stokkum, I. H. M.; Dekker, J. P.; van Grondelle, R.; Fleming, G. R. *J. Phys. Chem. B* **2001**, *105*, 4485.

(11) Byrdin, M.; Jordan, P.; Krauss, N.; Fromme, P.; Stehlik, D.; Schlodder, E. *Biophys. J.* **2002**, *83*, 433.

(12) Sener, M. K.; Lu, D.; Ritz, T.; Fromme, P.; Schulten, K. *J. Phys. Chem. B* **2002**, *106*, 7948.

(13) Yang, M.; Damjanovic, A.; Vaswani, H. M.; Fleming, G. R. *Biophys. J.* **2003**, *85*, 140.

(14) Damjanovic, A.; Vaswani, H. M.; Fromme, P.; Fleming, G. R. *J. Phys. Chem. B* **2002**, *106*, 10251.

(15) van Amerongen, H.; Valkunas, L.; van Grondelle, R. *Photosynthetic Excitons*; World Scientific Publishers: Singapore, 2000.

(16) Fragata, M.; Nordén, B.; Kurucsev, T. *Photochem. Photobiol.* **1988**, *47*, 133.

(17) van Zandvoort, M. A. M. J.; Wróbel, D.; Lettinga, P.; van Ginkel, G.; Levine, Y. K. *Photochem. Photobiol.* **1995**, *62*, 299.

(18) Kleima, F. J.; Hofmann, E.; Gobets, B.; van Stokkum, I. H. M.; van Grondelle, R.; Diederichs, K.; van Amerongen, H. *Biophys. J.* **2000**, *78*, 344.

(19) Parusel, A. B. J.; Grimme, S. *J. Phys. Chem. B* **2000**, *104*, 5395.

(20) Beddard, G. S. *J. Phys. Chem. B* **1998**, *102*, 10966.

(21) Beddard, G. S. *Philos. Trans. R. Soc. London, Ser. A* **1998**, *356*, 421.

(22) Renger, Th.; May, V.; Kühn, O. *Phys. Rep.* **2001**, *137*, 343.

(23) May, V.; Kühn, O. *Charge and Energy Transfer Dynamics in Molecular Systems*, 2nd ed.; Wiley-VCH: Berlin, 2004.

(24) Brüggemann, B.; May, V. *J. Chem. Phys.* **2004**, *120*, 2325.

(25) Houssier, C.; Sauer, K. *J. Am. Chem. Soc.* **1970**, *92*, 779.

(26) den Hartog, F. T. H.; van Papendrecht, C.; Störkel, U.; Völker, S. *J. Phys. Chem. B* **1999**, *103*, 1375.

(27) Peterman, E. J. G.; Pullerits, T.; van Grondelle, R.; van Amerongen, H. *J. Phys. Chem. B* **1997**, *101*, 4448.

(28) Mukamel, S. *Principles of Nonlinear Optical Spectroscopy*; Oxford University Press: Oxford, 1999.

(29) Gelin, M. F.; Egorova, D.; Domcke, W. *Chem. Phys.* **2004**, *129*, 301.

(30) Bäck, T.; Schwefel, H.-P. *Evolutionary Computation* **1993**, *1*, 1.

(31) Simonetto, R.; Crime, M.; Sandonà, D.; Croce, R.; Cinque, G.; Breton, J.; Bassi, R. *Biochemistry* **1999**, *38*, 12974.

(32) Zazubovich, V.; Matsuzaki, S.; Johnsson, T. W.; Hayes, J. M.; Chitnis, P. R.; Small, G. J. *Chem. Phys.* **2002**, *275*, 47.

(33) Jelezko, F.; Tietz, C.; Gerken, U.; Wrachtrup, J.; Bittl, R. *J. Phys. Chem. B* **2000**, *104*, 8093.

(34) If the considered exciton state is delocalized, the expansion coefficients $C_\alpha(m)$ are distributed across many sites m. According to the normalization of $C_\alpha(m)$, the sum $\sum_m |C_\alpha(m)|^4$ becomes small; thus, a large delocalization number $N(\alpha)$ follows. If we note $C_\alpha(m) \approx 1/\sqrt{N_{\mathrm{Chl}}}$ for a completely delocalized state where N_{Chl} is number of Chls in the complex, we get $N(\alpha) = N_{\mathrm{Chl}}$. In the contrary case of a localized exciton state, there are some larger $C_\alpha(m)$ which finally result in a small $N(\alpha)$. For a completely localized state we have $C_\alpha(m) = \delta_{m,m_0}$ which immediately results in $N(\alpha) = 1$.

(35) Holzwarth, A. R.; Schatz, G.; Brock, H.; Bittersmann, E. *Biophys. J.* **1993**, *64*, 1813.

(36) Byrdin, M.; Rimke, I.; Schlodder, E.; Stehlik, D.; Roelofs, T. A. *Biophys. J.* **2000**, *79*, 992.

(37) Novoderezhkin, V.; van Grondelle, R. *J. Phys. Chem. B* **2002**, *106*, 6025.

(38) Novoderezhkin, V.; Wendling, M.; van Grondelle, R. *J. Phys. Chem. B* **2003**, *107*, 11534.

(39) Brüggemann, B.; Herek, J. L.; Sundström, V.; Pullerits, T.; May, V. *J. Phys. Chem. B* **2001**, *105*, 11391.

(40) Novoderezhkin, V.; Salverda, J. M.; van Amerongen, H.; van Grondelle, R. *J. Phys. Chem. B* **2003**, *107*, 1893.

(41) Press, W. D.; Teukolsky, S. A.; Vetterling, W. T.; Flannery, B. P. *Numerical Recipies in Fortran*; Cambridge University Press: New York, 1992.

(42) Note that the fastest component splits up into two, one with a time constant of 414 fs and one with a time constant of 438 fs. Because they have a relatively large DAS, only the sum of both has been plotted. However, we did not comment on this effect in the running text because experimental data are not available for this short-time contribution.

(43) Brüggemann, B.; May, V. *Chem. Phys. Lett.* To be published.

(44) Brüggemann, B.; May, V. *J. Phys. Chem. B* (special issue honoring the work of Gerald J. Small) **2004**, *108*, 10529.